Incorporating Geostationary Lightning Data into a Radar Reflectivity Based Hydrometeor Retrieval Method: An Observing System Simulation Experiment

Haoliang Wang[1,2], Yubao Liu[2,3], Tianliang Zhao[1], Mei Xu[2], Yuewei Liu[2], Fengxia Guo[1], William Y.Y. Cheng[2], Shuanglei Feng[3], Edward R. Mansell[4], Alexandre O. Fierro[5]

[1] Collaborative Innovation Center on Forecast and Evaluation of Meteorological Disasters, Nanjing University of Information Science & Technology, Nanjing, China 210044

[2] National Center for Atmospheric Research, Boulder, Colorado, USA 80301

[3] China Electric Power Research Institute, Beijing, China 100192

[4] NOAA/OAR/National Severe Storms Laboratory, Norman, Oklahoma, USA 73072

[5] Cooperative Institute for Mesoscale Meteorological Studies, University of Oklahoma, and NOAA/OAR/National Severe Storms Laboratory, Norman, Oklahoma, USA 73072

Corresponding author: Haoliang Wang (haoliang@nuist.edu.cn).

Address: Nanjing University of Information Science & Technology, 210044 Ningliu Road, Nanjing, China 210044.

Manuscript submitted for consideration to *Atmospheric Research*

© 2018. This manuscript version is made available under the Elsevier user license
http://www.elsevier.com/open-access/userlicense/1.0/

Abstract

A retrieval method for deriving the hydrometeor mixing ratio within mesoscale convective system (MCS) is presented in this study. The hydrometeor retrieval method was designed to incorporate the flash extent densities (FED) data from the Feng-Yun-4 geostationary satellite into the S-band radar reflectivity (Z_h) and ambient temperature (T) data-based hydrometeor retrieval method. Total lightning data are utilized to better discern regions containing graupel in clouds. In the quantitative estimation of rain mixing ratio, different intercept parameters are used for different ranges of Z_h and different estimated precursors of raindrop in cold-cloud microphysical processes (i.e., graupel and snow aggregate). The hydrometeor retrieval method was evaluated through an observing system simulation experiment (OSSE) in which the pseudo-input-data for the hydrometeor retrieval (i.e., the FED, Z_h and T data) were obtained from the cloud-scale (1-km) simulation of an MCS using explicit electrification implemented within the Weather Research and Forecasting model. By incorporating the FED data as an additional input data source into the Z_h and T-based hydrometeor retrieval method, the hydrometeor retrieval accuracy was improved. The hydrometeor retrievals were then assimilated into the model using the Real-Time Four-Dimensional Data Assimilation (RTFDDA) system. Assimilating more accurate hydrometeor fields slightly improved the analyses and forecasts of convective precipitation in the test MCS case. The improvement could be due to the more accurate hydrometeor analysis, which further affected the strength of the cold pool and gust front.

Key words: Lightning; Hydrometeor retrieval; Data assimilation; Numerical weather prediction; Observing system simulation experiment.

1. Introduction

The retrieval of hydrometeor within convective clouds is useful to provide a more accurate estimate of latent heat release and to improve hydrometeor analyses for the initialization of convection-allowing numerical weather prediction (NWP) models, among other applications. These applications motivated several studies aimed at developing and testing hydrometeor retrieval methods (e.g., Dawson and Xue 2006; Hu and Xue 2007; Kain et al. 2010; Ziegler et al., 2013; Xue et al. 2014).

Owing to its high spatial and temporal resolution, weather radar remains the primary data source for hydrometeor retrieval. Previous studies have shown that polarimetric radars, which provide a variety of variables (e.g. reflectivity Z_h, differential reflectivity Z_{DR}, specific differential phase K_{DP}, and correlation coefficient ρ_{HV}), has the ability to identify bulk hydrometeor types of convective clouds and improve the quantitative estimate of liquid water content (LWC) and ice water content (IWC; e.g. Vivekanandan et al. 1999; Straka et al., 2000; Zrnic et al. 2001).

For areas solely within the range of non-polarimetric radars, reflectivity (Z_h) and temperature (T) based hydrometeor retrieval methods have been developed by several investigators (e.g., May et al., 2005; Hu et al., 2006; Lerach et al., 2010). The single Z_h

threshold (e.g., 32 dBZ c.f. Lerach et al., 2010; Pan et al., 2016) is often used to classify the graupel-dominated regions and snow aggregates-dominated regions above the freezing level. Because the possible ranges of Z_h for graupel and snow aggregates partially overlap (i.e., the Z_h range of graupel and snow aggregates are typically 25 – 50 dBZ and 0 – 35 dBZ, respectively; Straka et al., 2000), single Z_h threshold could introduce uncertainty in distinguishing the graupel-dominated versus snow aggregates-dominated regions. Cazenave et al. (2016) tested the sensitivity of the polarimetric radar-based classification of graupel and snow aggregates to the bias in Z_h, and found that a positive bias in Z_h of 3 dBZ changed the respective percentages of graupel-dominated regions and snow aggregates-dominated regions from 8% and 32.9% to 13.1% and 28.4% in the classification results of a squall line case, respectively. It can be inferred that the sensitivity of the classification of graupel-dominated regions and snow aggregates-dominated regions to the Z_h bias would be even larger without the additional information supplied by polarimetric radar variables (e.g., K_{DP} and Z_{DR}) in the simple Z_h and T-based hydrometeor retrieval method. Additionally, the classification of graupel-dominated and snow aggregates-dominated regions were found to be highly sensitive to the selected Z_h threshold in the Z_h and T-based hydrometeor retrieval method (include reference here).

It is generally accepted that the primary charge separation mechanism in thunderstorms arises from elastic collisions between graupel and ice crystals in the presence of supercooled water, known as riming electrification. This charging mechanism has been long supported by research based on laboratory experiments (e.g. Reynolds et al., 1957; Takahashi, 1978; Saunders et al., 1991;) and field observations (e.g., Dye et al., 1986; Lang et al., 2004; Qie et al., 2005a,b, 2009; MacGorman et al., 2005, 2008). Lightning discharge, which is a by-product of electrification and charge, is thus closely related to graupel content (e.g., Goodman et al., 1988; Carey and Rutledge, 1996, Fierro et al. 2006). Based on field observations, researchers found that the majority of lightning initiation occurs within or close to regions containing graupel (e.g. Bruning et al., 2007; Lund et al., 2009; Ribaud et al, 2016). Additionally, studies found that the regions without graupel (e.g., pure snow aggregates regions) are characterized by weak electric fields and lightning activity (Ribaud et al., 2016; Takahashi et al., 2017). These findings highlight the promising aspect of lightning data for indicating regions containing graupel.

Owing to recent developments of lightning detection technique, lightning data have been used as a proxy for rainfall (e.g., Alexander et al., 1999; Chang et al., 2001; Pessi and Businger, 2009), water vapor content (e.g., Fierro et al., 2012, 2014, 2015, 2016) and hydrometeor mixing ratio (e.g., Qie et al., 2014; Wang et al., 2017). China recently launched the Feng-Yun-4 (FY-4) geostationary satellite (Yang et al., 2016). One of the instruments aboard FY-4 is the Lightning Mapping Imager (LMI), which is able to detect total lightning (i.e., in-cloud plus cloud-to-ground flashes) over China and its adjacent regions with a spatial resolution of about 8-km at nadir with a detection efficiency nearing 90-% in real time (Yang et al., 2016). Most operational weather radars in China, however, are non-polarimetric, which imposes a stringent limitation for identifying graupel and snow aggregates. In this work, we demonstrate that the lightning data provided by the FY-4 geostationary satellite may, in some circumstances, help to improve the accuracy of the non-polarimetric radar based hydrometeor retrieval within mesoscale convective systems (MCSs).

This study presents a hydrometeor retrieval method, which incorporates the lightning data from the FY-4 geostationary satellite as an additional input data source into the Z_h and T based hydrometeor retrieval method. The hydrometeor retrieval method was evaluated via an observing system simulation experiment (OSSE). The impacts of the hydrometeor retrieval method on the short-term forecasts of an MCS at convection-resolving scale (1 km × 1 km) were evaluated through the use of the National Center for Atmospheric Research (NCAR) Real-Time Four-Dimensional Data Assimilation (RTFDDA) system.

2. Case description and model setup

2.1 Brief description of the severe convective event

An MCS, which took place in the North China Plain on 13 June 2010 was selected as the OSSE case. The MCS initially developed over the northwestern Hebei province around 0500 UTC and gradually moved southeastward toward Beijing around 1200 UTC. The MCS dissipated shortly before moving over the Bo Sea by 1800 UTC. The severe convective event lasted for more than 15 h. It was influenced by a deep low (996 hPa) situated over eastern Inner Mongolia. Convective available potential energy (CAPE) exceeded 2200 J/kg throughout much of Hebei, Beijing and Tianjin during this time, while convective inhibition (CIN) was overall weak (approximately -30 to -200 J/kg), indicating an environment favorable for severe convection.

2.2 Model setup

The numerical model used for this work is the Weather Research and Forecasting - Electrification (referred to as E-WRF; Mansell et al., 2005; Fierro et al., 2013) model. The simulation domains included two nested grids (Fig. 1). The horizontal grid spacings were 9 km, 3 km (i.e., convection-allowing scale) and 1 km (i.e., cloud-resolving scale) for each of the three domains, respectively. Hydrometeor retrieval and data assimilation were only performed in the innermost, cloud-resolving domain. Two-way nesting between parent and inner nests were activated, so the impact of data assimilation can feedback from the innermost cloud-resolving domain to its parent domains. Each domain features 43 vertical eta levels with a model top set at around 50 hPa. The “true simulation” used the ERA-Interim reanalysis produced by the European Centre for Medium-Range Weather Forecasts (ECMWF; Dee et al., 2011) as initial and lateral boundary conditions. The simulations were initialized at 0600 UTC, 0700 UTC, 0900 UTC for the D01, D02 and D03, respectively, and were ended at 0000 UTC, 14 June 2010. The initial fields for the nested domain were interpolated from their parent domain. The MCS was well captured by the innermost cloud-resolving domain (i.e., D03) during the entirety of the simulation (i.e., 15 hours).

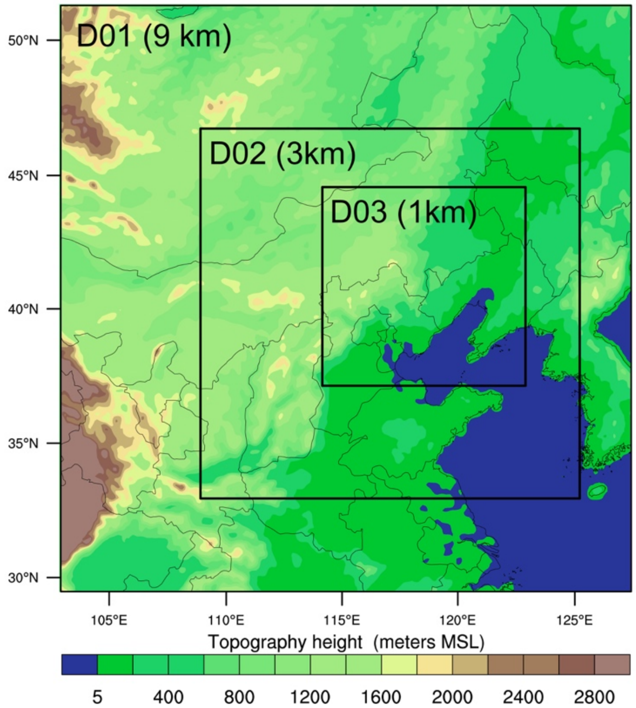

Fig. 1. Configuration of the WRF parent domain (D01: 9-km) and the two nested domains (D02: 3-km and D03: 1-km) for the OSSE case study. Terrain heights are shown in colored shades.

The physical schemes employed in this study included the NSSL double-moments bulk microphysics (Ziegler et al., 1985; Mansell et al., 2010a,b), the Noah land surface model (Chen and Dudhia 2001), the Mellor–Yamada–Janjic turbulence kinetic energy (TKE) scheme for the planetary boundary layer (Janjic 1994), and the Rapid Radiative Transfer Model GCMs (RRTMG) for shortwave and longwave radiation (Iacono et al., 2008). The Grell-Freitas convective parameterization scheme (CPS; Grell et al., 2013) was only activated in the parent domain (D01).

3. Methods

3.1 Simulated observations

The pseudo-LMI flash extent density (FED) observations were simulated using explicit electrification and lightning physics (Mansell et al., 2005; Fierro et al., 2013) which are coupled with the NSSL double-moment bulk microphysics scheme within WRF (E-WRF). The flash origin density and FED are explicitly simulated by E-WRF, which resolves the three-dimensional field of charge and solves for the three components of the ambient electric potential and, thus, ambient electric field. For more details on E-WRF, the reader is invited to consult Mansell et al. (2005) and Fierro et al. (2013). The areal extents of the simulated flash origin density were found to be reasonably consistent with the observations from the Earth Networks Total Lightning Network (ENTLN; Fierro et al., 2013).

In this set of simulations, the Saunders and Peck Scheme (Saunders and Peck, 1998; Mansell et al., 2005) was selected as the non-inductive charging scheme; for breakdown, the vertical electric field profile of Dwyer et al., (2003) was employed; the screening layer parameterization was de-activated; the size of the discharge cylinders was set to 6-km; the fraction of the net charge removed/superposed within the cylinder volumes upon bulk discharge was set to 60%.

The simulated 1-km FED were accumulated over a 15-min period and centered around the radar sampling time. The pseudo-LMI FED at each 8-km pixel was generated by selecting the maximum 1-km FED within the 8-km pseudo-LMI pixel (Fig. 2). The 8-km FED obtained using this approach likely are underestimated, as multiple lightning flashes could propagate into an 8-km pixel without overlapping each other on the 1-km pixel (Mansell et al., 2014). However, as the hydrometeor retrieval method presented in this study is essentially a binary function of lightning coverage, it is expected that the quantitative value of the FED fields has little impact on the retrieval results. The detection efficiency of the LMI was assumed as “perfect” for this study.

The pseudo-Z_h observation of S-band (λ = 10.5 cm) non-polarimetric radar reflectivity was simulated from the truth simulation by using a radar simulator coupled with the NSSL double-moments bulk microphysics scheme, which utilized the mixing ratios and number concentrations of rain, snow aggregates and graupel to calculate the equivalent reflectivity factor, Z_e (mm^6 m^{-3}; Ferrier et al., 1994; Mansell et al., 2010a). When a double-moment microphysics scheme is used, number concentration is allowed to vary independent of the mixing ratio, which can significantly improve the analysis of particle size distributions (PSD) and the computation of radar reflectivity. Cloud ice and cloud water were not considered when computing Z_e due to their negligible contributions. It was assumed that the effect of the 0 ℃ layer bright band has been corrected during the quality control process and the observations of Z_h were perfect. The Z_h data were interpolated from the radar polar coordinate onto the 1-km, Cartesian grid of D03.

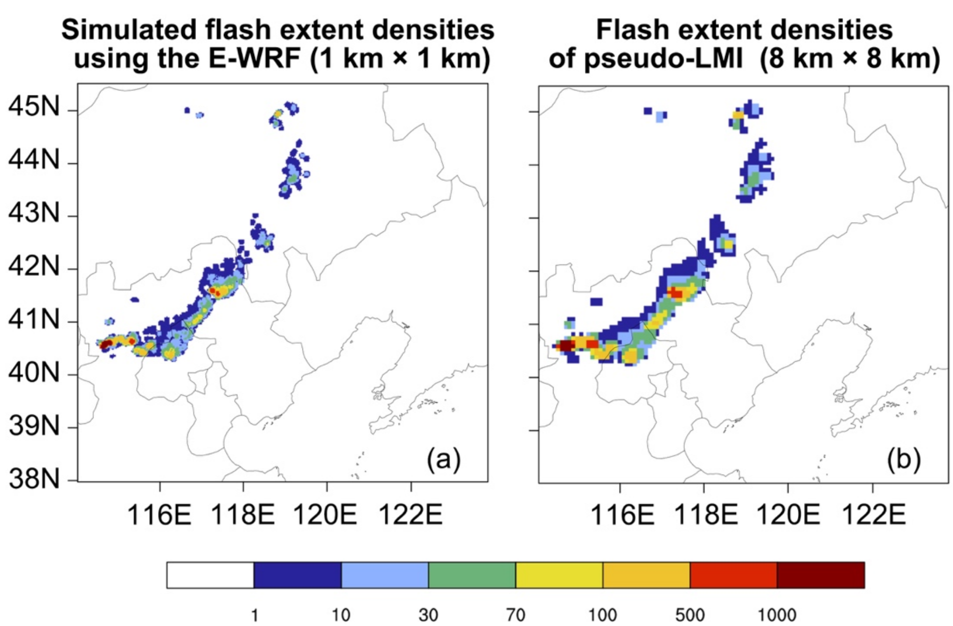

Fig. 2. Horizontal cross sections of (a) simulated FED fields in D03 (1×1 km^{-2}, 15 min^{-1}) and (b) the pseudo-LMI FED (8×8 km^{-2}, 15 min^{-1}).

3.2 Identification of the dominant hydrometeor type

The hydrometeor retrieval algorithm presented here is based on algorithms for non-polarimetric radar developed by Lerach et al. (2010), Gao et al. (2012) and Pan et al. (2016), which use the S-band Z_h and T. In the hydrometeor retrieval method presented here, the FED data were combined with Z_h and T to identify the hydrometeor type and to determine the intercept parameters of raindrop when quantitatively estimating rain mass mixing ratio (q_r).

The hydrometeor categories in the retrieval method contain rain, graupel and snow aggregates. The category of snow aggregates here refers to aggregated-ice and the category of graupel refers to rimed ice and heavily rimed snow, which is consistent with the definition in most bulk microphysical parameterization (BMP) schemes and dual-polarimetric radar based hydrometeor retrieval algorithms. Hail is not classified, as hail and graupel are not always explicitly treated separately in microphysics schemes.

Before describing the hydrometeor retrieval method, the information regarding which regions of a storm are favorable for frequent lightning initiation and propagation are introduced. The initiation and propagation of lightning is driven by the ambient electric field and electric potential, which are determined by the three-dimensional distribution of electric charge (e.g., Mansell et al., 2002, 2010a; Tan et al., 2014; Bruning et al., 2013; Wang et al., 2016). It is generally accepted that most of the electric charge in convective clouds is generated by the non-inductive mechanism, which requires the presence of graupel pellets. Therefore, it is reasonable to expect that lightning channels will follow the distribution of graupel particles, and graupel echo volume has been used as a proxy for lightning channel density (i.e., the FED; Allen et al., 2016). As convection matures, some charged ice crystals and snow aggregates are advected rearward into the anvil or trailing stratiform region (e.g., Carey et al., 2005) allowing some lightning flashes to propagate beyond the graupel regions in the updraft core into regions where the charge density is sufficient for continued propagation of lightning (e.g., Carey et al., 2005). Lightning can also occur in MCS stratiform regions and anvils of mature storms where graupel contents are low (Kuhlman et al., 2009). However, the FED rates in such regions generally are noticeably lower than in the vicinity of updraft cores (Carey et al., 2005; Calhoun et al., 2013). It was thus assumed that regions where the FEDs are significantly smaller than the average FED over the entire convective cell (F_AVG), would more likely be characterized by low charge density regions consisting of charged snow aggregates advected from the non-inductive electrification regions. The following approach was devised to filter the FED in those regions.

(i) In the FED map (8 km × 8 km), we clustered convective cell by using the accumulated FED data within a 15-min interval. If a pixel with non-zero FED is connected with other pixels with non-zero FED value, they are grouped into the same convective cell.

(ii) Computing the average FED for each clustered convective cell within a time window of 15-min (F_AVG).

(iii) Filtering the pixels with large negative deviations of FED from F_AVG. In this study, the pixels with FED less than 0.16·F_AVG were filtered out. We use the relative values instead of the absolute values as the filter parameter is designed to prevent the low FED convective cells from being filtered out. Since this filter threshold is somewhat arbitrary, it is challenging to exactly filter the low charge density regions consisting of charged ice crystals and snow aggregates advected from the non-inductive electrification regions. More accurate calibration of this parameter needs to be investigated in future study using real FED observations from the FY-4 geostationary satellite.

In order to jointly use the FED and Z_h data, the coverage of filtered 8-km FED was mapped onto the 1-km grid, i.e., if one 8-km pixel has a non-zero FED, all the 1-km pixels within that 8-km pixel will be assigned a non-zero FED value.

In the follow-on steps, graupel is classified in grid cells located in the cold cloud regions (T < 0 ℃), when one of the following criteria is met:

(i) The grid cell lies within the filtered FED outlines and $Z_h > 25$ dBZ.

(ii) The grid cell lies outside the filtered FED outlines and $Z_h > 35$ dBZ.

Similarly, snow aggregate is classified as follows:

(i) The grid cell lies within the filtered FED outlines and the 0 dBZ $< Z_h \leq$ 25 dBZ.

(ii) The grid cell lies outside the filtered FED outlines and the 0 dBZ $< Z_h \leq$ 35 dBZ.

The philosophy behind the choice of these particular criteria is that the regions inside the filtered FED outlines are those most likely to contain graupel particles. Therefore, the Z_h threshold used to differentiate between graupel and snow aggregates is set to the lower limit of the Z_h range of graupel (25 dBZ). For a time period of 15-min, the regions outside the filtered FED outlines are relatively less likely to contain graupel particles. In this case, the Z_h threshold used to differentiate between graupel and snow aggregates is set to the upper limit of the Z_h range of dry snow aggregates (35 dBZ), as Z_h hardly exceeds this threshold without the existence of graupel in cold-cloud regions.

The in-situ observations indicated that the regions of pure graupel are rare, and most cold-cloud regions consist of pure snow aggregates or mixed graupel/snow aggregates (e.g. Sukovich et al., 2009). Therefore, in cold-cloud regions, the grid cells identified as being dominated by graupel are regarded as mixed graupel/snow aggregates regions, and the grid cells identified as being dominated by snow aggregates are regarded as pure snow aggregates regions.

Because graupel and snow aggregates could coexist in the melting layer, their threshold temperatures are extended below the freezing level, namely: up to 5 ℃ and 3 ℃

respectively. The remaining hydrometeor species below the freezing level is classified as rain.

3.3 Quantitative estimations of hydrometeor mixing ratio

For the regions only containing one class of hydrometeor (e.g., pure rain or pure snow aggregates), the mixing ratio was simply computed using the Z_e-q equations. When multiple species coexist in the mixed regions, the measured total equivalent reflectivity factor (Z_e, mm^{6}m^{-3}) is partitioned and allotted to each hydrometeor species based on empirical observation results.

In the mixed graupel/snow aggregates regions, graupel and snow aggregates contribute to Z_e. The equivalent reflectivity factor of graupel ($\hat{Z}_e^{graupel}$) is computed as follows,

$$\hat{Z}_e^{graupel}(i,j,k) = p \cdot Z_e(i,j,k) \quad (1)$$

where $p\ (0 \leq p \leq 1)$ is the fraction of the Z_e from graupel.

Because graupel has a larger terminal fall speed than snow aggregate, it is reasonable to expect that graupel and snow aggregates in the mixed graupel/snow aggregates regions show differences in their vertical distribution. The trapezoidal weighting functions corresponding to ambient temperature profile for graupel and snow aggregates, which were used in Zrnic et al. (2001), were employed to consider the vertical distributions of graupel and snow aggregates. The equivalent reflectivity factor of graupel that takes into account the vertical distribution of graupel ($Z_e^{graupel}$) can be expressed as:

$$Z_e^{graupel}(i,j,k) = \frac{p \cdot W_{graupel}[T(k)]}{p \cdot W_{graupel}[T(k)] + (1-p) \cdot W_{snow}[T(k)]} \cdot Z_e(i,j,k) \quad (2)$$

where i, j, k represent the horizontal and vertical coordinate dimensions, $T(k)$ is the ambient temperature profile, and $W_{graupel}[T(k)]$ and $W_{snow}[T(k)]$ are the trapezoidal weighting functions (between 0 and 1) corresponding to ambient temperature profile for graupel and snow aggregates.

The equivalent reflectivity factor of snow aggregates (Z_e^{snow}) in the mixed graupel/snow aggregates regions is computed as follows:

$$Z_e^{snow}(i,j,k) = \frac{(1-p) \cdot W_{snow}[T(k)]}{p \cdot W_{graupel}[T(k)] + (1-p) \cdot W_{snow}[T(k)]} \cdot Z_e(i,j,k) \quad (3)$$

In convective clouds, the fraction of graupel in the mixed graupel/snow aggregates regions varies from case to case. Here, we assumed p is 0.9 in the mixed graupel/snow regions. The upper limit of Z_e^{snow} was set to 10$^{3.5}$ mm^6 m^{-3}, as the Z_h for snow aggregates hardly exceeds 35 dBZ (e.g., Straka et al., 2000). If the calculated Z_e^{snow} exceeded 10$^{3.5}$ mm^{6}m^{-3}, the grid cells were reallocated to graupel. The graupel mixing ratio (q_g) and snow aggregates mixing ratio (q_s) in the mixed graupel/snow aggregates regions were computed using Z_e-q relationships where $Z_e^{graupel}$ and Z_e^{snow} were determined.

In the melting layer, q_g and q_s were estimated using a linear function with their values at the cold-cloud regions used as the starting value. Because it was assumed that the effects of the bright band near the freezing level has been corrected during the quality control, the graupel and snow aggregates were assumed to be dry. The Z_e^{rain} in the melting layer was calculated after subtracting the $Z_e^{graupel}$ and Z_e^{snow}.

When using Z_e-q relationship to quantitatively estimate the hydrometeor mixing ratio, the PSD were assumed to be exponential shape (Eq. 4).

$$N_x(D) = N_{0x}\exp(-\lambda_x D_x) \quad (4)$$

where x represents the hydrometeor species (i.e., graupel, snow aggregates, rain), $N_x(D)\delta D$ is the drop numbers per unit volume between diameters D and $D+\delta D$, N_{0x} is the intercept parameter, which is the value of N_x for $D=0$, λ_x is the slope parameter, which is diagnosed as

$$\lambda_x = \left(\frac{\rho_x \pi N_{0x}}{\rho q_x}\right)^{0.25} \quad (5)$$

where ρ_x is the bulk density of hydrometeor, ρ is the air density, and q_x is the hydrometeor mixing ratio.

The intercept parameters and the densities of graupel and snow aggregates (Table 1) were assumed constant. Although this assumption was used in previous studies (e.g., Xue et al., 2006; Tong et al., 2008), it is important to highlight that there exist uncertainties in these assumptions, as the PSD varies significantly in space and time.

Table 1. A summary of the intercept parameters and bulk densities of each hydrometeor categories used in the hydrometeor retrieval method.

Categories	Intercept parameter (m^{-4})	Density (kg m^{-3})
Graupel	3×10^6	400
Snow aggregates	2×10^7	100
Rain	8×10^6 / Variable	1000

The relationship between the Z_h for rain computed using the double-moment microphysics parameters (i.e., mixing ratio and number concentration) and q_r were analyzed throughout the life cycle of a simulated MCS (Fig. 3). It was found that with the increase of Z_h^{rain}, q_r tended to be overestimated when the intercept parameter of rain (N_{0r}) was set to 8×10^6 m^{-4}, which value has been widely used for representing raindrop PSD (e.g., Lin et al. 1983; Hong et al. 2004). When N_{0r} was set to 3×10^6 m^{-4}, such overestimation was partially alleviated (Fig. 3). This is consistent with past studies that the high Z_h regions are more likely to be associated with relatively low number concentrations, which is an indication of larger drop size (e.g., Schuur et al. 2001; Carlin et al., 2016). Cold rain processes contribute significantly to the total rainfall within MCS (e.g. Houze et al., 1997). The other factor that affects raindrop size was found to be the precursor of raindrop in cold cloud microphysical processes (e.g., Waldvogel et al., 1974;

Fabry and Zawadzki, 1995). In the case of equal Z_h value, raindrops resulting from the melting of snow aggregates tend to have a larger size than those which melted from graupel (e.g., Waldvogel et al., 1974).

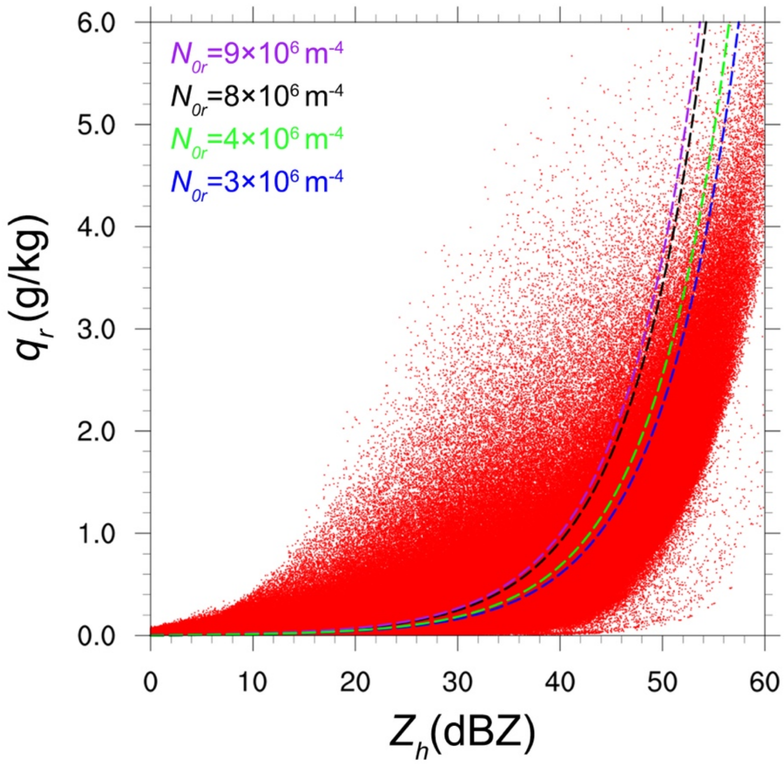

Fig. 3. Comparison of the Z_e-q equation (Z_e is converted to Z_h herein) for raindrops when assuming an exponential shape PSD (Eq. 4) with different N_{0r} (dash curves) and q_r versus Z_h from rain (red dots) computed using the double-moment microphysics parameters throughout the life cycle of the simulated MCS. The formulae used to compute Z_h from rain with the double-moment microphysics parameters was the same as in the radar simulator coupled in the NSSL double-moments bulk microphysics scheme. The values of N_{0r} corresponding to each curve are marked with colored font.

Infused from these findings, N_{0r} was not assumed constant in this hydrometeor retrieval method.

(i) In the column where only snow aggregates exist above 0 ℃:

$$N_{0r} = \begin{cases} 8 \times 10^6 m^{-4}; 0 < Z_h \leq 35 \text{ dBZ} \\ (43 - Z_h) \times 10^6 m^{-4}; \ 35 < Z_h \leq 40 \text{ dBZ} \\ 3 \times 10^6 m^{-4}; Z_h > 40 \text{ dBZ} \end{cases}$$

(ii) Similarly, in the column where graupel exists above 0 ℃:

$$N_{0r} = \begin{cases} 9 \times 10^6 m^{-4}; 0 < Z_h \leq 35 \text{ dBZ} \\ (44 - Z_h) \times 10^6 m^{-4}; \ 35 < Z_h \leq 40 \text{ dBZ} \\ 4 \times 10^6 m^{-4}; Z_h > 40 \text{ dBZ} \end{cases}$$

Since the slope of the rain PSD is proportional to N_{0r}, decreasing N_{0r} shifts the peak of raindrops PSD towards bigger drops. The best-fitted relationship between N_0 and Z_h was not derived using the model simulations, as such a relationship is sensitive to the microphysics scheme used.

4. Results

4.1 The evaluation of the hydrometeor retrieval method

To evaluate the effects of incorporating FED as an additional data source into the Z_h and T based hydrometeor retrieval method, two main experiments were devised namely, "FED-Z_hT" wherein FED, Z_h and T are used in the hydrometeor retrieval and "Z_hT " where only Z_h and T are used via the OSSE approach. For Z_hT, the thresholds used to identify hydrometeor types were the same as in Lerach et al. (2010), e.g., the snow aggregates and graupel were segregated using a fixed Z_h threshold of 32 dBZ.

The simulated FED, Z_h and T from the true simulation were used as the input data for FED-Z_hT and Z_hT. The hydrometeor retrievals were performed every 15-min starting when the simulated MCS began to produce lightning at 1-h forecast. The retrieved hydrometeor mixing ratios (i.e. q_r, q_g, q_s) from the two different retrieval methods were compared to those from the true simulation. The evolution of the MCS in the true simulation is shown in Fig. 4.

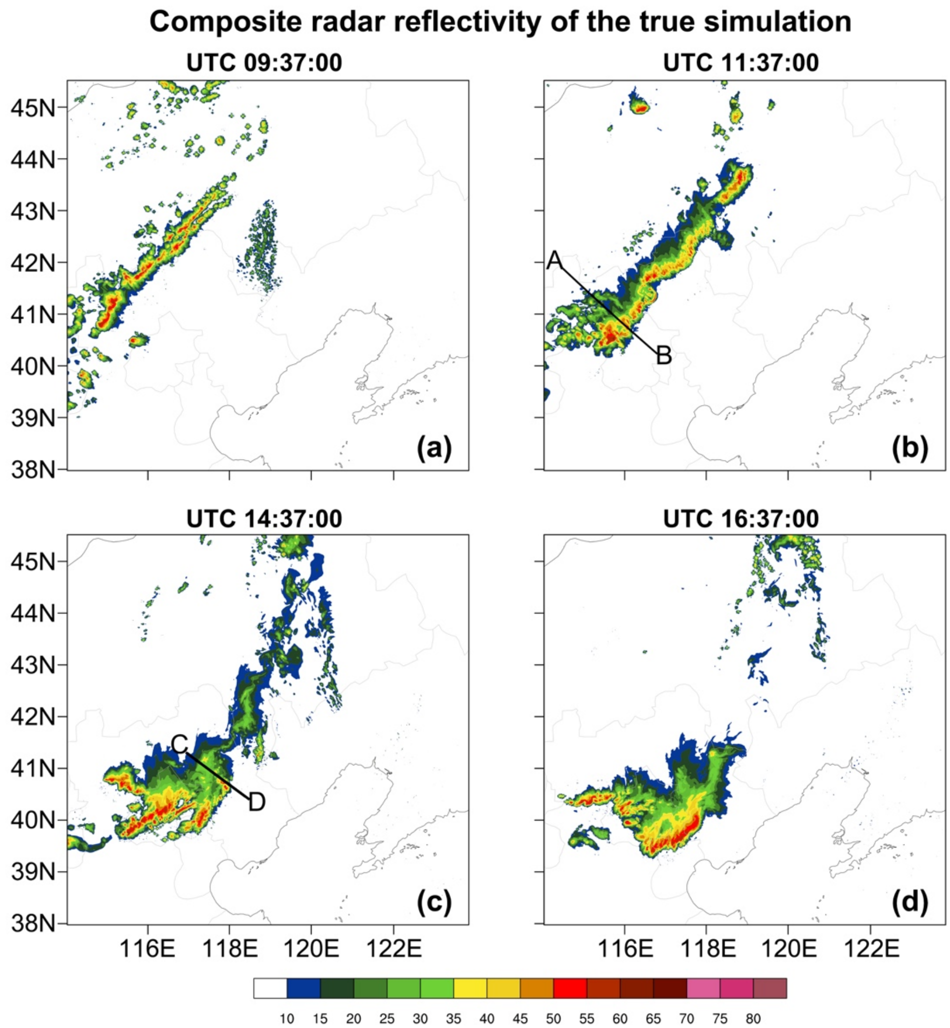

Fig. 4. Composite radar reflectivity fields of the true simulation on D03. The valid forecast time is shown above each panel. The black lines in (b) and (c) indicate the locations of the vertical cross sections shown in Fig. 4 and Fig. 5.

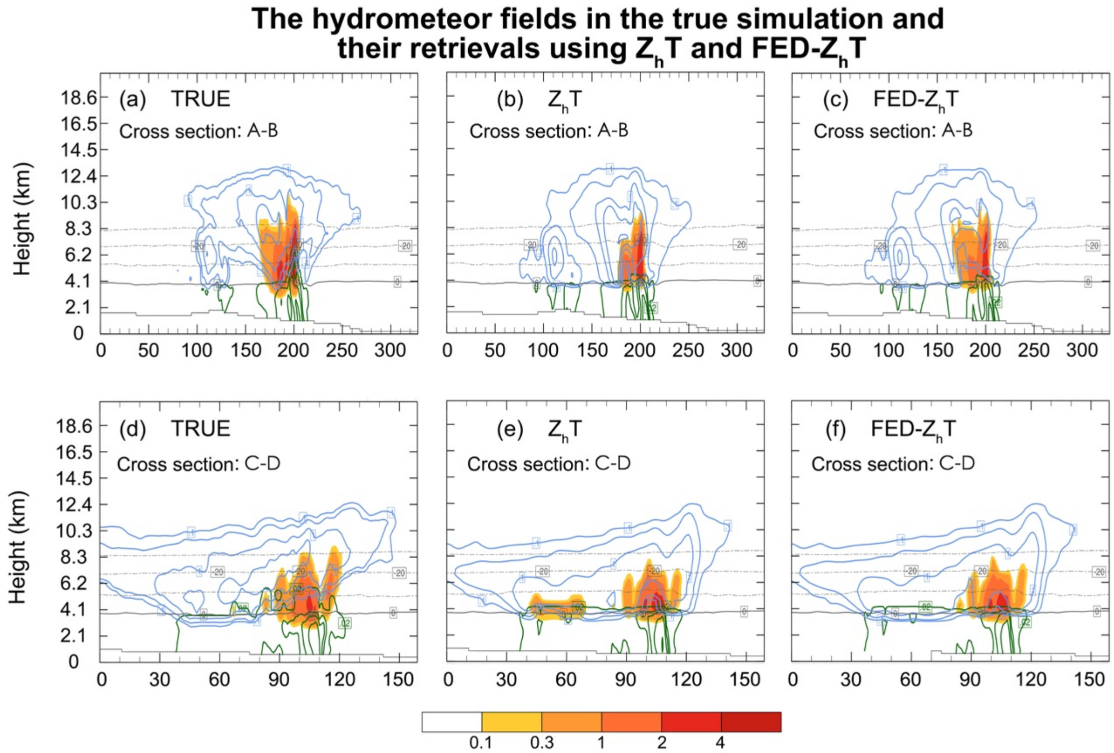

Fig. 5. Vertical cross-sections of the hydrometeor mixing ratio fields: q_g (color shadings), q_s (blue contours), q_r (green contours) from (a), (d) true simulation; (b), (e) Z_hT and (c), (f) FED-Z_hT. Legend for the color shadings for q_g (g kg^{-1}) is shown on the bottom. The contour intervals of q_s (g kg^{-1}) are 0.1, 0.3, 1.0, 2.0, 4.0. The contour intervals of q_r (g kg^{-1}) are 0.02, 0.5, 1.0, 2.0, 4.0. The locations of the vertical cross sections are denoted by the black lines in Figs. 4.

In general, the regions of rain, graupel and snow aggregates were reasonably well classified by Z_hT (Figs. 5b,e). The areal extents of some graupel regions, however, were smaller than those in the true simulation (Figs. 5b), as Z_h of the regions consisting of small graupel particles might be less than 32 dBZ, which was the threshold used to identify the graupel-dominated regions in the Z_hT. In FED-Z_hT, a relatively lower Z_h threshold was employed in lightning regions for identifying areas containing graupel particles. Overall, this approach improved the graupel estimations (Figs. 5c,f). The snow aggregates regions where Z_h exceeded 32 dBZ were misidentified as graupel regions in Z_hT (Fig. 5e). In FED-Z_hT, the relatively higher Z_h threshold for identifying graupel was applied in the regions outside the filtered FED outlines, which reduced the misidentification of graupel (Fig. 5f). As a result, the retrieval biases of graupel in Z_hT were alleviated in some cases in FED-Z_hT (Fig. 6).

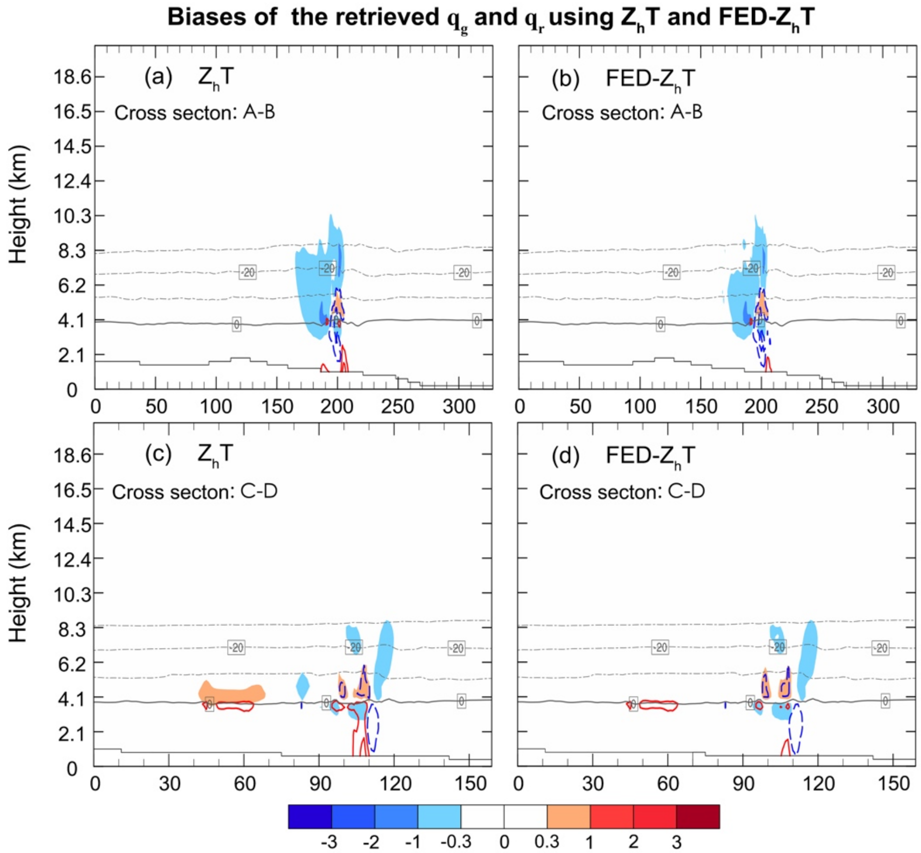

Fig. 6. Vertical cross-sections of the biases in the retrievals of q_g (color shadings), q_r (red and blue contours) relative to the true simulation values for (a), (c) Z_hT and (b), (d) FED-Z_hT. A positive value indicates overestimation, and vice versa. Legend for the color shadings (g kg^{-1}) is shown on the bottom. Red solid (blue dash) contours denote positive (negative) values (g kg^{-1}) at intervals of ±0.3, ±1, ±2, ±3 respectively. The locations of the vertical cross sections are the same as in Figs. 5.

In convective clouds, in-situ observations from aircraft revealed that supercooled raindrops can often be lofted above 0 ℃ up to -10 ℃ by sufficiently strong updrafts (e.g., Brandes et al., 1995; Bringi et al., 1997). This observation was corroborated by the discovery of "Z_{DR} columns" above 0 ℃ with polarimetric radars (e.g., Conway and Zrnić, 1993). In the true simulation, it was found that the raindrops were lofted above 0 ℃, while the raindrops above 0 ℃ were neglected in both Z_hT and FED-Z_hT, which resulted in an underestimation of q_r above 0 ℃ (Fig. 6). Past studies found that suprercooled raindrops between 0 ℃ and -10 ℃ typically have large size (e.g. Hubbert et al. 1998; Carlin et al., 2016), and thus have a significant contribution to Z_h. When raindrops were neglected above 0 ℃, the Z_h contribution from the raindrops is allocated to graupel and snow aggregates, which resulted in overestimations of q_g and q_s where supercooled raindrops should exist (Fig. 6).

In the regions below 0 ℃, the primary source of error in the retrieval of q_r originates from the variations of raindrop size. In the Z_hT, a constant N_{0r} was used in the

Z_e-q retrieval equation for rain. This resulted in a noteworthy overestimation of q_r in some regions (Figs. 6a,c) due to the existence of large size raindrops. By employing a variable N_{0r} to account for the variations of the raindrop size in different regions, the overestimation of q_r retrievals were reduced (Figs. 6b,d).

To quantify the performance of FED-Z_hT, the equitable threat score (ETS, Clark et al. 2010) and frequency bias (BIAS) were computed for the retrievals of q_g, q_s and q_r from the FED-Z_hT and Z_hT, respectively. When computing the ETS and BIAS, the true simulation was regarded as the reference. The ETS and BIAS were computed at different mass mixing ratio thresholds (0.1, 0.3, 0.6, 1.0, 2.0, 3.0 g kg^{-1}) for the entire domain (D03) over the entire duration of the simulation.

The ETS in Clark et al. (2010) is calculated using four parameters, namely: “Hits” (the number of correct forecasts of occurrence), “Misses” (the number of occurrences which were missed by forecast), False Alarms (the number of false forecasts of nonoccurrence), and Correct Rejections (the number of correct forecasts of nonoccurrence), as below:

$$ETS = \frac{Hits + Chance}{Hits + Misses + False\ Alarms - Chance}$$

where,

$$Chance = \frac{(Hits + False\ Alarms)(Hits + Misses)}{Hits + Misses + False\ Alarms + Correct\ Rejections}$$

The ETS ranges between 0 to 1, where 0 indicates no skill, and 1 indicates perfect skill. The equation to compute the BIAS is:

$$BIAS = \frac{Hits + False\ Alarms}{Hits + Misses}$$

A BIAS above (below) 1, indicates that the algorithm over(under)-estimates the mass mixing ratios.

Before analyzing the quantitative evaluations of the retrievals, it is useful to re-iterate the major sources of the error in hydrometeor retrieval, namely: (i) The misidentification of the dominant hydrometeor type; (ii) the uncertainties in the assumed intercept parameters and bulk densities of hydrometeors, which were used in the Z_e-q equations and (iii) the fraction assumptions of each class of hydrometeor in the mixed-hydrometeor regions (e.g., the mixed graupel/snow aggregates regions) in the retrieval method.

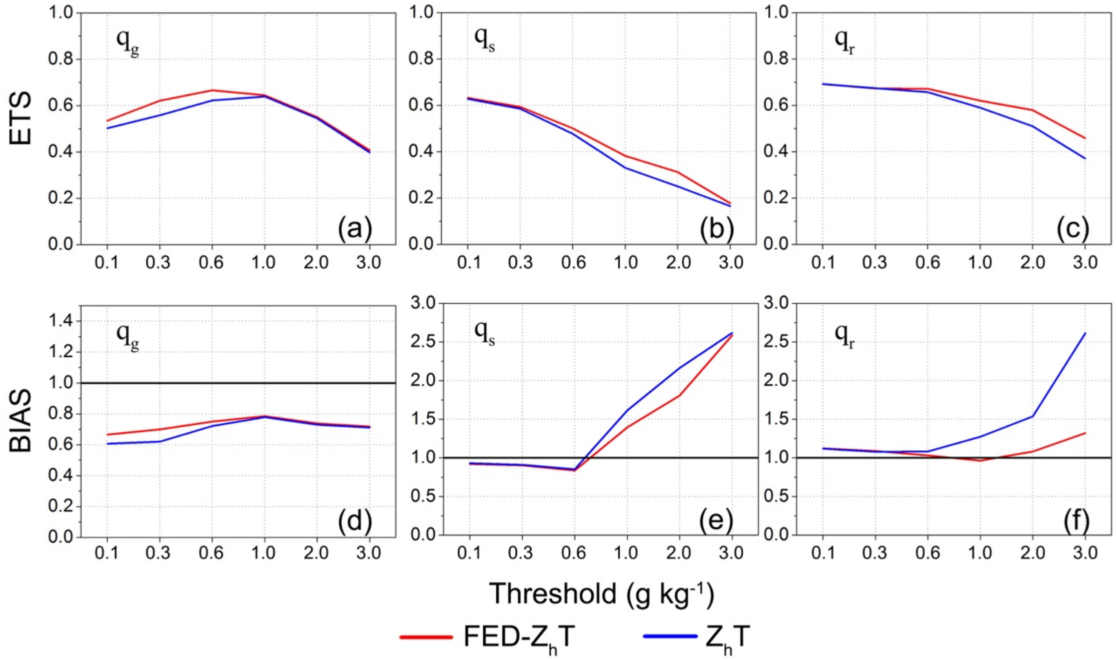

Fig. 7. The ETS and BIAS at different thresholds for the retrievals of (a), (d) q_g; (b), (e) q_s; (c), (f) q_r for FED-Z_hT (in red) and Z_hT (in blue) relative to the true simulation.

The retrievals of q_g in FED-Z_hT are associated with higher ETS compared to Z_hT (Figs. 7a,d), which was traced back to FED-Z_hT having more "Hits" and less "False Alarms" (not shown). The improvement was mainly seen for thresholds ranging between 0.1 and 0.6 g kg^{-1}, as the graupel particles, which have similar Z_h to snow aggregates, typically have small q_g. A systematic underestimation of qg was still present in FED-Z_hT, which could be caused by the uncertainties in the assumed intercept parameter and bulk density of graupel used in the Z_e-q equation and the fraction assumptions. Compared with the retrievals of q_g and q_r, the retrievals of q_s exhibits relatively lower ETS at most thresholds in both methods (Figs. 7b,e), as more uncertainties existed in the PSD of snow aggregates (Zhang et al., 2016). The improvement of q_s retrievals was mainly seen for thresholds exceeding 1 g kg^{-1}, as the snow aggregates, which have similar Z_h to graupel particles, typically have large q_s.

For a given value of Z_h, snow aggregates exhibited a higher ice water content (IWC) than graupel, due to the differences in their respective PSDs. If graupel particles were mistakenly classified as snow aggregates (i.e., "Miss" event of graupel), the IWC would be overestimated, and vice versa. The BIAS of q_g and q_s (Figs. 7a,b,d,e) indicate that the FED-Z_hT alleviated more "Misses" than "False Alarms" of graupel (what about qs?). As a result, the overall IWC in the retrievals with Z_hT were larger than those of FED-Z_hT (not shown).

When assuming a variable N_{0r}, the ETS of q_r was improved relative to the experiment using a constant N_{0r}.This improvement was mainly seen for thresholds above 0.6 g kg^{-1} (Figs. 7c,f). The q_r above 0.6 g kg^{-1} was systematically overestimated with Z_hT, while such overestimation was reduced in FED-Z_hT.

4.2 Short-term forecasts with the data assimilation of hydrometeor retrievals

To test the effects of the improved hydrometeor retrievals on the short-term forecast of the MCS, the hydrometeor retrievals using Z_hT and FED-Z_hT were respectively assimilated into the model using the NCAR WRF-RTFDDA system. This data assimilation (DA) tool makes use of Newtonian relaxation nudging based on four-dimensional data DA. There are two types of DA methods currently implemented in WRF-RTFDDA (Stauffer and Seaman, 1990; Liu et al., 2006): the observation nudging and grid nudging. The grid nudging method was designed to assimilate three-dimensional data with high temporal-spatial resolution. In the grid nudging, background fields are nudged toward the observations/analyses at the corresponding analysis-model grid points, following Eq. (6):

$$\frac{\partial X_g}{\partial t} = P(X_g, t) + G_X \cdot T_X \cdot (Y_g - X_g) \quad (6)$$

where X_g is the model-state variable, $P(X_g, t)$ is the model original prognostic equation, G_X is the relaxation time scale used to reduce noise induced by instantaneous change of the model fields, T_X is a time weight, which is a function of the time lags between the observation and model state, Y_g is the observation or analysis value on the model grids.

When assimilating the mixing ratio of each class of the hydrometeor, the corresponding latent heat releases were also computed and assimilated into the model using the latent heat nudging module of WRF-RTFDDA.

The true simulation used here was the same as in Section 2.2. The configurations of the control (no DA) and the DA experiment were the same as in the true simulation except for the initial conditions. The initial conditions of the control and the DA run were generated by randomly perturbing the ERA-Interim reanalysis at the initial time. The perturbations were obtained by a stochastic sampling the background error covariance from the WRF-DA (Barker et al. 2004), and were applied to the air temperature, wind, and water vapor. The descriptions and acronyms of all the experiments are summarized in Table 2. In ASML-Z_hT and ASML-FZ_hT, the hydrometeor retrievals were continuously assimilated in the innermost domain for 2-h from the initialization of that domain at 0900 UTC. From the end of the analysis at 1100 UTC, 4-h forecasts were performed in each experiment.

Table 2. The descriptions and acronyms of each set of forecast experiment.

Experiment names	Initial condition	Data used for hydrometeor retrieval	Descriptions
TRUE	ERA-Interim reanalysis	\	True simulation
CTRL	ERA-Interim reanalysis with a random perturbation	\	Control run without data assimilation
ASML-Z_hT	The same as in CTRL	Z_h, T	Data assimilation run using the hydrometeor retrievals from Z_h and T
ASML-FZ_hT	The same as in CTRL	FED, Z_h, T	Data assimilation run using the hydrometeor retrievals from FED, Z_h and T

Since precipitation is an accumulated field, while radar reflectivity is instantaneous, it is expected that precipitation will be more sensitive to the analysis of hydrometeor fields compared to radar reflectivity. Therefore, the hourly precipitation for each experiment was analyzed (Fig. 8). Overall, both assimilation experiments (i.e., ASML-Z_hT and ASML-FZ_hT) performed better than CTRL, indicating that assimilating the observation-based hydrometeor retrievals can improve short-term precipitation forecast of this MCS. The displacement errors in CTRL were reduced in the assimilation experiments. The areal coverage of the MCS was smaller in CTRL. The northwestern portion of the precipitation field of the MCS was absent in CTRL (Figs. 8a,b,e,f), due to weak temperature gradients coupled with ,marginal convergence there (Fig. 9b). In the assimilation experiments, appreciable updrafts were induced in those regions through latent heat nudging (Fig. 10c). The assimilated hydrometeors produced more rainfall there, which resulted in a stronger cool pool and outflow front (Figs. 9c,d). The outflow front continuously lifted the warmer and moister air ahead of it, sustaining convection there. During the forecast, both assimilation experiments exhibit weaker rainfall amounts relative to the true simulation to the southwest, but have larger rainfall to the northeast (Figs. 8i,k,l). This cloud be explained by the humidity field in the initial conditions (Fig. 10): by the end of the analysis time, the air ahead of the southwest portion of the MSC was drier in the assimilation experiments than in the true simulation, while the air ahead of the northeast portion of the MSC was moister in the assimilation experiments compared to the true simulation (Figs. 10a,c). These humidity biases at larger scales did have a pronounced effect on the accumulated precipitation forecasts in the assimilation experiments.

In the analysis period, the morphology and location of the MCS in ASML-FZ_hT were similar to those of ASML-Z_hT. The convective precipitation of ASML-Z_hT, however, was stronger than in ASML-FZ_hT and presented a lager bias than ASML-FZ_hT when taking the true simulation as the reference (Figs. 8a,c,d). This was partly due to the analysis fields in ASML-Z_hT exhibiting higher LWC and IWC, as explained in Section 3.1. Additionally, the latent heat releases were proportional to the increments of LWC and IWC, which resulted in larger temperature increments in ASML-Z_hT, and a correspondingly stronger thermodynamic forcing. Other background fields would also be adjusted through the kinematic and microphysics to accommodate the changes in thermodynamic forcing. Compared to ASML-Z_hT, the convective region of the analysis fields in ASML-FZ_hT contained more graupel, which was more prone to precipitate than snow aggregate. Snow aggregate, however, could gradually undergo riming wherever supercooled water subsisted, to eventually convert into graupel. In summary, ASML-Z_hT could produce more precipitable ice due to the overestimation of the IWC and the gradual riming of snow aggregates.

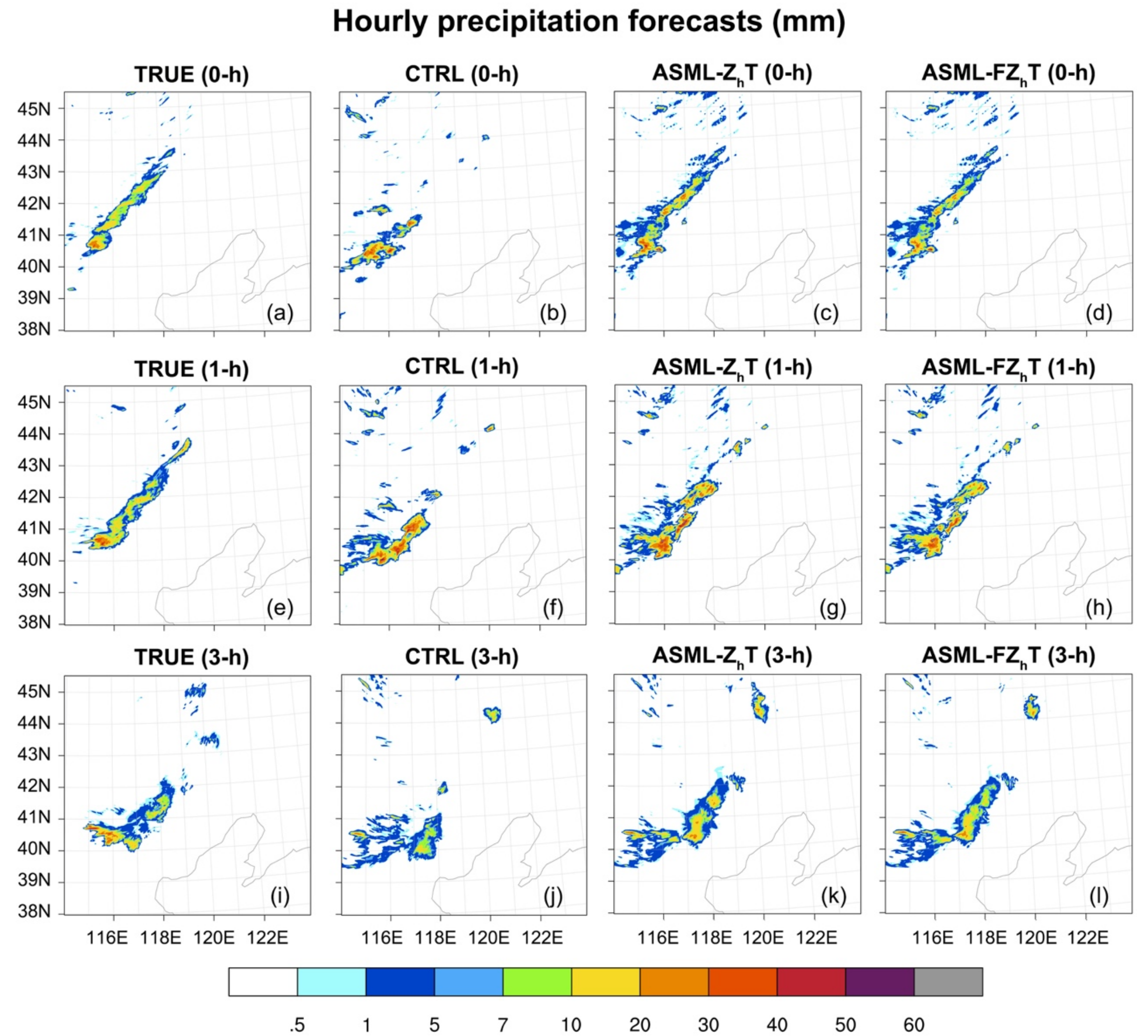

Fig. 8. Hourly accumulated precipitation rates (mm) for (a), (e), (i): TRUE; (b), (f), (j): CTRL; (c), (g), (k): ASML-Z$_h$T; and (d), (h), (l): ASML-FZ$_h$T. The valid forecast time is shown above each panel with 0-h representing the last hour of the analysis time.

During the forecast period, although the hydrometeor analyses were no longer assimilated, ASML-Z$_h$T still produced heavier rainfall and larger rainfall maxima than ASML-FZ$_h$T and TRUE (Figs. 8e-l). This could be explained by the stronger cold pool and gust front in ASML-Z$_h$T (Figs. 9c,d), which were associated with heavier precipitation in the analysis period, and, thus, deeper cold pool (e.g., Gilmore and Wicker 1998; Fierro et al., 2008). The strengthening of the initial cold pool yielded a positive feedback with the precipitation fields (Figs. 9g,h).

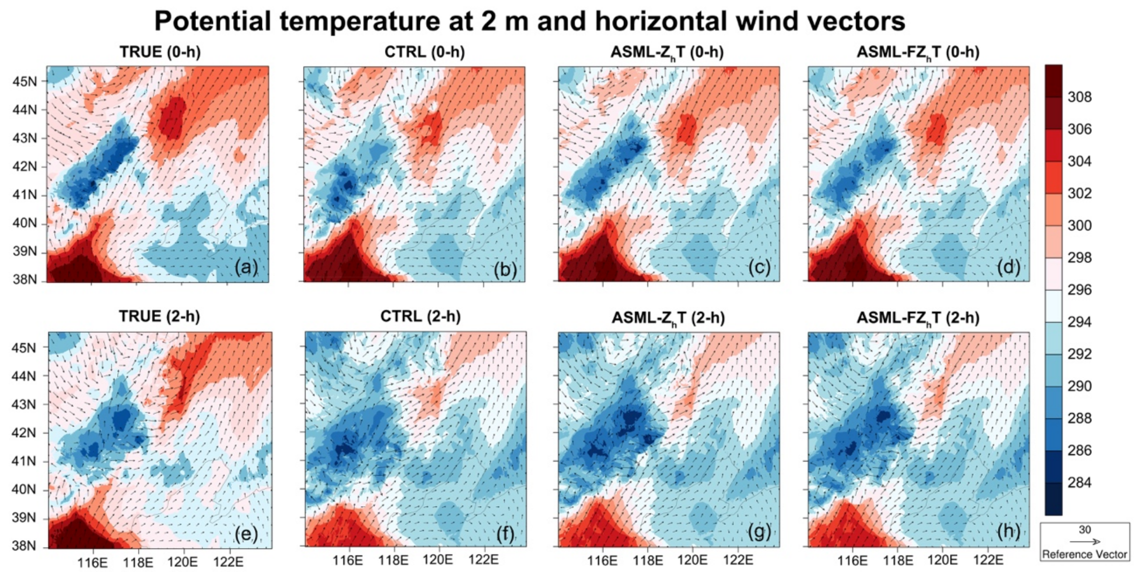

Fig. 9. 2-m potential temperature fields (shading; K) overlaid with the 850-hPa horizontal wind (wind arrows; m s^{-1}) for (a), (e): TRUE; (b), (f): CTRL; (c), (g): ASML-Z$_h$T; (d), (h): ASML-FZ$_h$T. The forecast time is shown above each panel with 0-h representing the end of the analysis time.

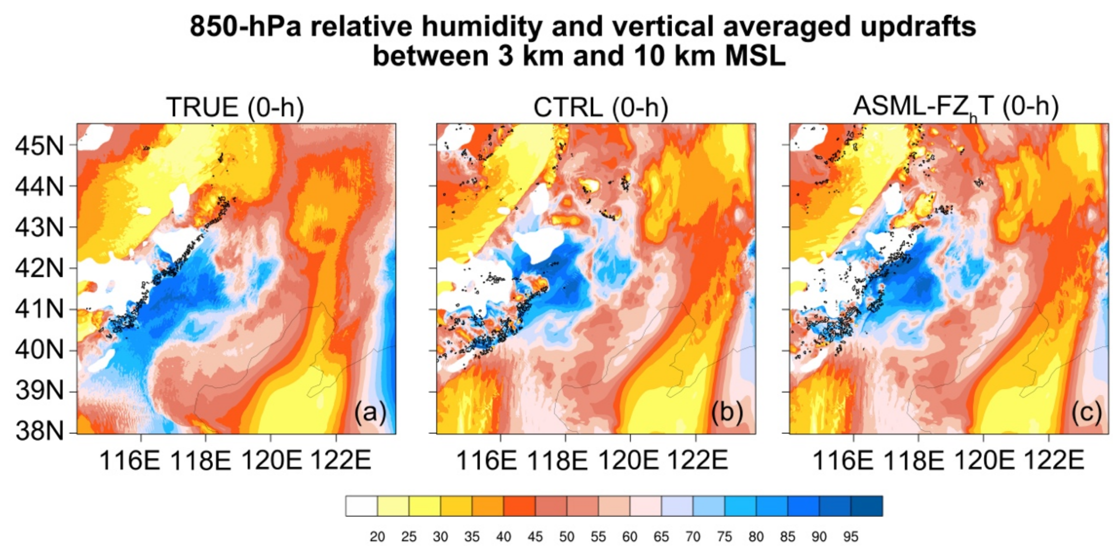

Fig. 10. 850-hPa relative humidity fields (shading; %) overlaid with the averaged vertical velocities between 3 km and 10 km MSL (black contours; contour of 2 m s^{-1}) for (a): TRUE; (b): CTRL and (c): ASML-FZ$_h$T at the end of the analysis time.

To quantitatively compare the precipitation forecast of different experiments, the Fractions Skill Score (FSS, Roberts and Lean, 2008) at different thresholds and different neighborhood radii from 1 – 30 km (i.e., 1 – 30 neighborhood grid cells) were calculated for hourly-accumulated precipitation forecasts for each experiment. Since the FSS is more tolerant to small displacement errors compared to the ETS, it is more appropriate for the evaluation of the simulation with fine resolution grids (e.g., Fierro et al. 2015). The precipitation from the true simulation was regarded as the reference when computing the FSS for each experiment. For the sake of brevity, only the results for the 15-km neighborhood radius at the rainfall thresholds of 2.5 and 10 mm were presented herein (Fig. 11). In general, the assimilation experiments (i.e., ASML-Z_hT, ASML-FZ_hT) achieved higher FSS compared to CTRL at all thresholds in both the analysis and forecast periods (Fig. 11). CTRL produced a low FSS, due to the large displacement errors of the simulated MCS, as well as the selected small neighborhood radius for the FSS computation. The more accurate analysis of the hydrometeor fields in ASML-FZ_hT resulted in slightly higher FSS compared with ASML-Z_hT. The improvement was clearer at the threshold of 10 mm (Fig. 11b) compared to 2.5 mm (Fig. 11a), indicating the improvement of hydrometeor analysis had more impact on the forecast of convective precipitation than those of stratiform precipitation.

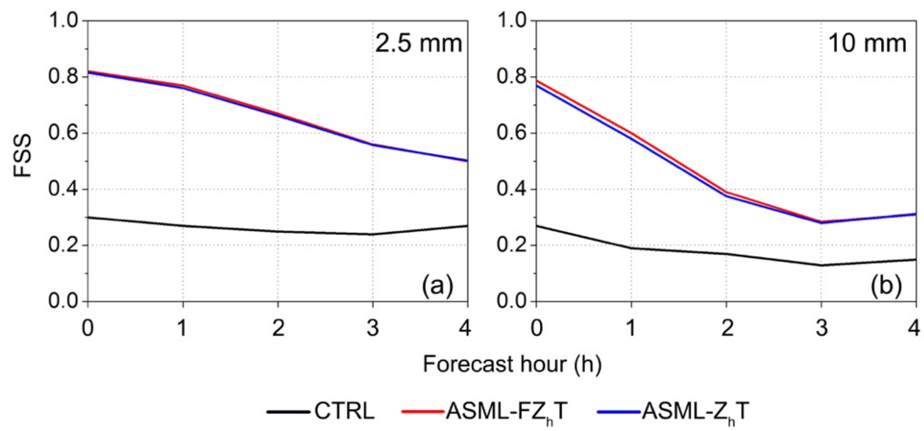

Fig. 11. FSS of the hourly-accumulated precipitation forecasts for the thresholds of (a) 2.5 mm; (b) 10 mm for CTRL (in black), ASML-FZ_hT (in red) and ASML-Z_hT (in blue). This evaluation begins at the last hour of the analysis time.

5. Conclusions

This study presents a hydrometeor retrieval method, which combines S-band Z_h, T and FED data. The hydrometeor retrieval method is based on those proposed by Lerach et al. (2010), Gao et al. (2012) and Pan et al. (2016), who employed S-band Z_h and ambient T to retrieve hydrometeors. Since the ranges of Z_h of graupel and snow aggregates are partially overlapping, uncertainties exist in distinguishing the graupel-dominated and snow aggregates-dominated regions when only using Z_h and T data. The hydrometeor retrieval method presented in this study incorporates lightning data into the Z_h and T based hydrometeor retrieval algorithm. Lightning data are utilized to better discern regions containing graupel in clouds. Different Z_h thresholds are then applied to different regions to identify the graupel-dominated and snow aggregates-dominated regions. For the quantitative estimation of q_r, different N_{0r} are used for different ranges of Z_h and different estimated precursors of raindrop in cold-cloud microphysical processes (i.e., graupel or snow aggregate).

The hydrometeor retrieval method was tested with the observing system simulation experiment (OSSE) in which the input data for the hydrometeor retrieval (i.e., the FED, Z_h and T data) were obtained from a MCS simulation using explicit electrification implemented in the WRF model, which couples an explicit charging and bulk discharge lightning scheme in the NSSL double-moment microphysics, at cloud-resolving scale (1-km). By incorporating the FED as additional input data source into the Z_h and T based hydrometeor retrieval method, the hydrometeor retrieval accuracy was improved. However, uncertainties still existed in the quantitative retrieval of hydrometeor mixing ratio, which primarily arise from the assumptions behind the hydrometeor PSD and the fraction of each class of hydrometeor in the mixed-hydrometeor regions. The graupel PSD may evolve in response to changing lightning rate, as both the graupel PSD and total lightning rate are related to the updraft strength. For example, decreasing total lightning rate may indicate the decrease of updraft strength, which may shift the peak of the graupel PSD towards the smaller particles. The relationship between graupel PSD and total lightning rate could be incorporated into the lightning data based-hydrometeor retrieval method when such relationships are better understood, which remains the subject of future research endeavors.

The hydrometeor retrievals (with and without lightning information) were respectively assimilated into WRF using the NCAR-RTFDDA assimilation and forecast system. Both of the assimilation experiments performed better than the control experiment. Assimilating the hydrometeor retrievals with the added information from lightning slightly improved the analyses and forecasts of precipitation in a test MCS case. Overall, the improvement was more pronounced for the convective precipitation. The improvement could be due to the more accurate hydrometeor analysis, which further affected the strength of cold pool and gust front. The cold pool and gust front feedbacked with the subsequent evolution of MCS by impacting the storm thermodynamic environment. Because the evolution of convective systems is affected by complex nonlinear processes, future research should be devoted to the testing and evaluation of additional cases, preferably spanning different regimes.

The current lightning-based hydrometeor retrieval method is not expected to serve as a surrogate for hydrometeor retrieval methods based on polarimetric radar, which contains a larger wealth of information to infer the characteristics of hydrometeor species. For instance, when using polarimetric radar based hydrometeor retrieval method, Z_{DR} above 0 ℃ can be used to indicate the existence of supercooled raindrops (e.g., Kumjian and Ryzhkov 2008); Z_{DR} and K_{DP} can be used to estimate the Z_h associated with rain and perceptible ice particles in the mixed-phase region, respectively, (e.g., Carey et al., 2000). Achieving such level of detail is beyond the capabilities of the current lightning-based hydrometeor retrieval method. Until present, however, most of the operational weather radars in China have not yet been upgraded to polarimetric technology, and under the circumstances that the real-time nationwide detection of lightning will be provided by the recently-launched FY-4 geostationary satellite, it is expected that incorporating total lightning data into the non-polarimetric radar-based hydrometeor retrieval methods could add value to the hydrometeor retrieval and short-term forecast of MCS at small additional expenses. Because only case was analyzed with an OSSE, this study should be viewed as a “proof-of-concept” for a tentative lightning based hydrometeor retrieval method.

Consequently, the applicability of this method to realistic settings (i.e., non-OSSE) requires further testing with real observation data, namely: the FED data from the FY-4 geostationary satellite, dual-polarimetric radar data, and other surface based datasets.

Acknowledgments

This work was supported by the State Grid Corporation of China under the Sciences and Technology Project: SGTYHT/14-JS-188, the Postgraduate Research and Innovation Projects of Jiangsu Province: KYLX16_0939, the National Key Basic Research Program of China: Grant No. 2014CB441403. We would like to acknowledge high-performance computing support from Yellowstone (ark:/85065/d7wd3xhc) provided by NCAR's Computational and Information Systems Laboratory, sponsored by the National Science Foundation. ERA-Interim data provided courtesy ECMWF.

References

Alexander, G.D., Weinman, J.A., Karyampudi, V.M., Olson, W.S. and Lee, A.C.L., 1999. The effect of assimilating rain rates derived from satellites and lightning on forecasts of the 1993 superstorm. Mon. Wea. Rev. 127(7), 1433-1457.

Allen, B.J., Mansell, E.R., Dowell, D.C. and Deierling, W., 2016. Assimilation of pseudo-GLM data using the ensemble Kalman filter. Mon. Wea. Rev. 144(9), 3465-3486.

Barker, D.M., Huang, W., Guo, Y.R., Bourgeois, A.J. and Xiao, Q.N., 2004. A three-dimensional variational data assimilation system for MM5: Implementation and initial results. Mon. Wea. Rev. 132(4), 897-914.

Brandes, E.A., Vivekanandan, J., Tuttle, J.D. and Kessinger, C.J., 1995. A study of thunderstorm microphysics with multiparameter radar and aircraft observations. Mon. Wea. Rev. 123(11), 3129-3143.

Bringi, V.N., Knupp, K., Detwiler, A., Liu, L., Caylor, I.J. and Black, R.A., 1997. Evolution of a Florida thunderstorm during the Convection and Precipitation/Electrification Experiment: The case of 9 August 1991. Mon. Wea. Rev. 125(9), 2131-2160.

Bruning, E.C. and MacGorman, D.R., 2013. Theory and observations of controls on lightning flash size spectra. J. Atmos. Sci. 70(12), 4012-4029.

Bruning, E.C., Rust, W.D., Schuur, T.J., MacGorman, D.R., Krehbiel, P.R. and Rison, W., 2007. Electrical and polarimetric radar observations of a multicell storm in TELEX. Mon. Wea. Rev. 135(7), 2525-2544.

Calhoun, K.M., MacGorman, D.R., Ziegler, C.L. and Biggerstaff, M.I., 2013. Evolution of lightning activity and storm charge relative to dual-Doppler analysis of a high-precipitation supercell storm. Mon. Wea. Rev. 141(7), 2199-2223.

Carey, L. D., & Rutledge, S. A., 1996. A multiparameter radar case study of the microphysical and kinematic evolution of a lightning producing storm. Meteorol. Atmos. Phys. 59(1-2), 33-64.

Carey, L.D. and Rutledge, S.A., 2000. The relationship between precipitation and lightning in tropical island convection: A C-band polarimetric radar study. Mon. Wea. Rev. 128(8), 2687-2710.

Carey, L.D., Murphy, M.J., McCormick, T.L. and Demetriades, N.W., 2005. Lightning location relative to storm structure in a leading line, trailing stratiform mesoscale convective system. J. Geophys. Res. Atmos. 110(D3).

Carlin, J.T., Ryzhkov, A.V., Snyder, J.C. and Khain, A., 2016. Hydrometeor Mixing Ratio Retrievals for Storm-Scale Radar Data Assimilation: Utility of Current Relations and Potential Benefits of Polarimetry. Mon. Wea. Rev. 144(8), 2981-3001.

Cazenave, F., Gosset, M., Kacou, M., Alcoba, M., Fontaine, E., Duroure, C. and Dolan, B., 2016. Characterization of hydrometeors in Sahelian convective systems with an X-band radar and comparison with in situ measurements. Part I: Sensitivity of polarimetric radar particle identification retrieval and case study evaluation. J. Appl. Meteor. Climatol. 55(2), 231-249.

Chang, D.E., Weinman, J.A., Morales, C.A. and Olson, W.S., 2001. The effect of spaceborne microwave and ground-based continuous lightning measurements on forecasts of the 1998 Groundhog Day storm. Mon. Wea. Rev. 129(8), 1809-1833.

Chen, F., and Dudhia J., 2001. Coupling an Advanced Land Surface–Hydrology Model with the Penn State–NCAR MM5 Modeling System, Part I: Model Implementation and Sensitivity. Mon. Wea. Rev., 129, 569–585, doi:10.1175/1520- 0493(2001)129<0569:caalsh>2.0.co;2.

Clark, A. J., Gallus Jr, W. A., & Weisman, M. L., 2010. Neighborhood-based verification of precipitation forecasts from convection-allowing NCAR WRF model simulations and the operational NAM. Wea. and Forecasting, 25(5), 1495-1509.

Conway, J.W. and Zrnić, D.S., 1993. A study of embryo production and hail growth using dual-Doppler and multiparameter radars. Mon. Wea. Rev. 121(9), 2511-2528.

Dawson, D.T. and Xue, M., 2006. Numerical forecasts of the 15–16 June 2002 Southern Plains mesoscale convective system: impact of mesoscale data and cloud analysis. Mon. Wea. Rev. 134(6), 1607-1629.

Dee, D.P., Uppala, S.M., Simmons, A.J., Berrisford, P., Poli, P., Kobayashi, S., Andrae, U., Balmaseda, M.A., Balsamo, G., Bauer, P. and Bechtold, P., 2011. The ERA-Interim reanalysis: Configuration and performance of the data assimilation system. Q. J. Roy. Meteor. Soc. 137(656), 553-597.

Dye, J.E., Jones, J.J., Winn, W.P., Cerni, T.A., Gardiner, B., Lamb, D., Pitter, R.L., Hallett, J. and Saunders, C.P.R., 1986. Early electrification and precipitation development in a small, isolated Montana cumulonimbus. J. Geophys. Res. Atmos. 91(D1), 1231-1247.

Fabry, F. and Zawadzki, I., 1995. Long-term radar observations of the melting layer of precipitation and their interpretation. J. Atmos. Sci. 52(7), 838-851.

Ferrier, B. S. (1994). A double-moment multiple-phase four-class bulk ice scheme. Part I: Description. Journal of the Atmospheric Sciences, 51(2), 249-280.

Fierro, A. O., Gilmore, M. S., Mansell, E. R., Wicker, L. J., & Straka, J. M., 2006. Electrification and lightning in an idealized boundary-crossing supercell simulation of 2 June 1995. Mon. Wea. Rev. 134(11), 3149-3172.

Fierro, A.O., Leslie, L.M., Mansell, E.R. and Straka, J.M., 2008. Numerical simulations of the microphysics and electrification of the weakly electrified 9 February 1993 TOGA COARE squall line: Comparisons with observations. Mon. Wea. Rev. 136(1), 364-379.

Fierro, A.O., Mansell, E.R., Ziegler, C.L. and MacGorman, D.R., 2012. Application of a lightning data assimilation technique in the WRF-ARW model at cloud-resolving scales for the tornado outbreak of 24 May 2011. Mon. Wea. Rev. 140(8), 2609-2627.

Fierro, A.O., Mansell, E.R., MacGorman, D.R. and Ziegler, C.L., 2013. The implementation of an explicit charging and discharge lightning scheme within the WRF-ARW model: Benchmark simulations of a continental squall line, a tropical cyclone, and a winter storm. Mon. Wea. Rev. 141(7), 2390-2415.

Fierro, A. O., Gao, J., Ziegler, C. L., Mansell, E. R., MacGorman, D. R., & Dembek, S. R., 2014. Evaluation of a cloud-scale lightning data assimilation technique and a 3DVAR method for the analysis and short-term forecast of the 29 June 2012 derecho event. Monthly Weather Review, 142(1), 183-202.

Fierro, A.O., Clark, A.J., Mansell, E.R., MacGorman, D.R., Dembek, S.R. and Ziegler, C.L., 2015. Impact of storm-scale lightning data assimilation on WRF-ARW precipitation forecasts during the 2013 warm season over the contiguous United States. Mon. Wea. Rev. 143(3), 757-777.

Fierro, A.O., Gao, J., Ziegler, C.L., Calhoun, K.M., Mansell, E.R. and MacGorman, D.R., 2016. Assimilation of Flash Extent Data in the Variational Framework at Convection-Allowing Scales: Proof-of-Concept and Evaluation for the Short-Term Forecast of the 24 May 2011 Tornado Outbreak. Mon. Wea. Rev. 144(11), 4373-4393.

Gao, J. and Stensrud, D.J., 2012. Assimilation of reflectivity data in a convective-scale, cycled 3DVAR framework with hydrometeor classification. J. Atmos. Sci. 69(3), 1054-1065.

Gilmore, M.S. and Wicker, L.J., 1998. The influence of midtropospheric dryness on supercell morphology and evolution. Mon. Wea. Rev. 126(4), 943-958.

Goodman, S. J., Buechler, D. E., Wright, P. D., and Rust, W. D., 1988. Lightning and precipitation history of a microburst-producing storm. Geophys. Res. Lett. 15(11), 1185-1188.

Grell, G. A., and Freitas, S. R., 2013. A scale and aerosol aware stochastic convective parameterization for weather and air quality modeling, Atmos. Chem. Phys, 2014, 14(10): 5233-5250. doi:10.5194/acpd-13-23845-2013.

Hong, S.Y., Dudhia, J. and Chen, S.H., 2004. A revised approach to ice microphysical processes for the bulk parameterization of clouds and precipitation. Mon. Wea. Rev. 132(1), pp.103-120.

Houze Jr, R.A., 1997. Stratiform precipitation in regions of convection: A meteorological paradox?. Bull. Amer. Meteor. Soc. 78(10), 2179-2196.

Hu, M., Xue, M. and Brewster, K., 2006. 3DVAR and cloud analysis with WSR-88D level-II data for the prediction of the Fort Worth, Texas, tornadic thunderstorms. Part I: Cloud analysis and its impact. Mon. Wea. Rev. 134(2), 675-698.

Hu, M. and Xue, M., 2007. Implementation and evaluation of cloud analysis with WSR 88D reflectivity data for GSI and WRF ARW. Geophys. Res. Lett. 34(7).

Hubbert, J., Bringi, V.N., Carey, L.D. and Bolen, S., 1998. CSU-CHILL polarimetric radar measurements from a severe hail storm in eastern Colorado. J. Appl. Meteor. 37(8), 749-775.

Iacono, M. J., J. S. Delamere, E. J. Mlawer, M. W. Shephard, S. A. Clough, and Collins, W. D., 2008. Radiative forcing by long-lived greenhouse gases: Calculations with the AER radiative transfer models, J. Geophys. Res. Atmos., 113, doi:10.1029/2008jd009944.

Janjić, Z. C. A. I., 1994. The Step-Mountain Eta Coordinate Model: Further Developments of the Convection, Viscous Sublayer, and Turbulence Closure Schemes, Mon. Wea. Rev., 122, 927–945, doi:10.1175/1520-0493(1994)122<0927:tsmecm>2.0.co;2.

Kain, J.S., Dembek, S.R., Weiss, S.J., Case, J.L., Levit, J.J. and Sobash, R.A., 2010. Extracting unique information from high-resolution forecast models: Monitoring selected fields and phenomena every time step. Wea. Forecasting 25(5), 1536-1542.

Kuhlman, K.M., MacGorman, D.R., Biggerstaff, M.I. and Krehbiel, P.R., 2009. Lightning initiation in the anvils of two supercell storms. Geophys. Res. Lett. 36(7).

Kumjian, M.R. and Ryzhkov, A.V., 2008. Polarimetric signatures in supercell thunderstorms. J. Appl. Meteor. Climatol. 47(7), 1940-1961.

Lang, T.J., Miller, L.J., Weisman, M., Rutledge, S.A., Barker III, L.J., Bringi, V.N., Chandrasekar, V., Detwiler, A., Doesken, N., Helsdon, J. and Knight, C., 2004. The severe thunderstorm electrification and precipitation study. Bull. Amer. Meteor. Soc. 85(8), 1107-1125.

Lerach, D.G., Rutledge, S.A., Williams, C.R. and Cifelli, R., 2010. Vertical structure of convective systems during NAME 2004. Mon. Wea. Rev. 138(5), 1695-1714.

Lin, Y.L., Farley, R.D. and Orville, H.D., 1983. Bulk parameterization of the snow field in a cloud model. J Clim. Appl. Meteorol. 22(6), 065-1092.

Liu, Y., Chen, F., Warner, T. and Basara, J., 2006. Verification of a mesoscale data-assimilation and forecasting system for the Oklahoma City area during the Joint Urban 2003 field project. J. Appl. Meteor. Climatol. 45(7), pp.912-929.

Lund, N.R., MacGorman, D.R., Schuur, T.J., Biggerstaff, M.I. and Rust, W.D., 2009. Relationships between lightning location and polarimetric radar signatures in a small mesoscale convective system. Mon. Wea. Rev. 137(12), 4151-4170.

MacGorman, D.R., Rust, W.D., Krehbiel, P., Rison, W., Bruning, E. and Wiens, K., 2005. The electrical structure of two supercell storms during STEPS. Mon. Wea. Rev. 133(9), 2583-2607.

MacGorman, D.R., Rust, W.D., Ziegler, C.L., Mansell, E.R., Schuur, T.J., Biggerstaff, M.I., Straka, J.M., Bruning, E.C., Kuhlman, K.M., Lund, N.R. and Payne, C., 2008. TELEX the thunderstorm electrification and lightning experiment. Bull. Amer. Meteor. Soc. 89(7), 997-1013.

Mansell, E.R., MacGorman, D.R., Ziegler, C.L. and Straka, J.M., 2002. Simulated three dimensional branched lightning in a numerical thunderstorm model. J. Geophys. Res. Atmos. 107(D9).

Mansell, E.R., MacGorman, D.R., Ziegler, C.L. and Straka, J.M., 2005. Charge structure and lightning sensitivity in a simulated multicell thunderstorm. J. Geophys. Res. Atmos. 110(D12).

Mansell, E.R., Ziegler, C.L. and Bruning, E.C., 2010a. Simulated electrification of a small thunderstorm with two-moment bulk microphysics. J. Atmos. Sci. 67(1), 171-194.

Mansell, E.R., 2010b. On sedimentation and advection in multimoment bulk microphysics. J. Atmos. Sci. 67(9), 3084-3094.

Mansell, E.R., 2014. Storm-scale ensemble Kalman filter assimilation of total lightning flash-extent data. Mon. Wea. Rev. 142(10), 3683-3695.

May, P.T. and Keenan, T.D., 2005. Evaluation of microphysical retrievals from polarimetric radar with wind profiler data. J. Appl. Meteor. 44(6), 827-838.

Pan, Y., Xue, M. and Ge, G., 2016. Incorporating diagnosed intercept parameters and the graupel category within the ARPS cloud analysis system for the initialization of double-moment microphysics: Testing with a squall line over south China. Mon. Wea. Rev. 144(1), 371-392.

Pessi, A.T. and Businger, S., 2009. Relationships among lightning, precipitation, and hydrometeor characteristics over the North Pacific Ocean. J. Appl. Meteor. Climatol. 48(4), 833-848.

Qie, X., Kong, X., Zhang, G., Zhang, T., Yuan, T., Zhou, Y., Zhang, Y., Wang, H. and Sun, A., 2005a. The possible charge structure of thunderstorm and lightning discharges in northeastern verge of Qinghai–Tibetan Plateau. Atmos. Res. 76(1), 231-246.

Qie, X., Zhang, T., Chen, C., Zhang, G., Zhang, T. and Wei, W., 2005b. The lower positive charge center and its effect on lightning discharges on the Tibetan Plateau. Geophys. Res. Lett. 32(5).

Qie, X., Zhang, T., Zhang, G., Zhang, T., Kong, X., 2009. Electrical characteristics of thunderstorms in different plateau regions of China. Atmos. Res. 91 (2–4), 244–249.

Qie, X., Zhu, R., Yuan, T., Wu, X., Li, W. and Liu, D., 2014. Application of total-lightning data assimilation in a mesoscale convective system based on the WRF model. Atmos. Res. 145, 255-266.

Reynolds, S.E., Brook, M. and Gourley, M.F., 1957. Thunderstorm charge separation. Journal of Meteorology, 14(5), 426-436.

Ribaud, J.F., Bousquet, O. and Coquillat, S., 2016. Relationships between total lightning activity, microphysics and kinematics during the 24 September 2012 HyMeX bow echo system. Q. J. Roy. 142(S1), 298-309.

Roberts, N.M. and Lean, H.W., 2008. Scale-selective verification of rainfall accumulations from high-resolution forecasts of convective events. Mon. Wea. Rev. 136(1), 78-97.

Saunders, C.P.R. and Peck, S.L., 1998. Laboratory studies of the influence of the rime accretion rate on charge transfer during crystal/graupel collisions. J. Geophys. Res. Atmos. 103(D12), 13949-13956.

Saunders, C.P.R., Keith, W.D. and Mitzeva, R.P., 1991. The effect of liquid water on thunderstorm charging. J. Geophys. Res. Atmos. 96(D6), 11007-11017.

Schuur, T.J., Ryzhkov, A.V., Zrnić, D.S. and Schönhuber, M., 2001. Drop size distributions measured by a 2D video disdrometer: Comparison with dual-polarization radar data. J. Appl. Meteor. 40(6), 1019-1034.

Stauffer, D.R. and Seaman, N.L., 1990. Use of four-dimensional data assimilation in a limited-area mesoscale model. Part I: Experiments with synoptic-scale data. Mon. Wea. Rev. 118(6), 1250-1277.

Straka, J.M., Zrnić, D.S. and Ryzhkov, A.V., 2000. Bulk hydrometeor classification and quantification using polarimetric radar data: Synthesis of relations. J. Appl. Meteor. 39(8), 1341-1372.

Sukovich, E.M., Kingsmill, D.E. and Yuter, S.E., 2009. Variability of graupel and snow observed in tropical oceanic convection by aircraft during TRMM KWAJEX. J. Appl. Meteor. Climatol. 48(2), 185-198.

Takahashi, T., 1978. Riming electrification as a charge generation mechanism in thunderstorms. J. Atmos. Sci. 35(8), 1536-1548.

Takahashi, T., Sugimoto, S., Kawano, T. and Suzuki, K., 2017. Riming Electrification in Hokuriku Winter Clouds and Comparison with Laboratory Observations. J. Atmos. Sci. 74(2), 431-447.

Tan, Y., Tao, S., Liang, Z. and Zhu, B., 2014. Numerical study on relationship between lightning types and distribution of space charge and electric potential. J. Geophys. Res. Atmos. 119(2), 1003-1014.

Tong, M. and Xue, M., 2008. Simultaneous estimation of microphysical parameters and atmospheric state with simulated radar data and ensemble square root Kalman filter. Part I: Sensitivity analysis and parameter identifiability. Mon. Wea. Rev. 136(5), 1630-1648.

Vivekanandan, J., Ellis, S.M., Oye, R., Zrnic, D.S., Ryzhkov, A.V. and Straka, J., 1999. Cloud microphysics retrieval using S-band dual-polarization radar measurements. Bull. Amer. Meteor. Soc. 80(3), 381-388.

Waldvogel, A., 1974. The N 0 jump of raindrop spectra. J. Atmos. Sci. 31(4), 1067-1078.

Wang, H., Guo, F., Zhao, T., Qin, M. and Zhang, L., 2016. A numerical study of the positive cloud-to-ground flash from the forward flank of normal polarity thunderstorm. Atmos. Res. 169, 183-190.

Wang, H., Liu, Y., Cheng, W., Zhao, T., Xu, M., Shen, S., Calhoun, K.M., 2017. Improving Lightning and Precipitation Prediction of Severe Convection using Lightning Data Assimilation with NCAR WRF-RTFDDA. J. Geophys. Res. Atmos. 122(22), 12296-12316.

Xue, M., Tong, M. and Droegemeier, K.K., 2006. An OSSE framework based on the ensemble square root Kalman filter for evaluating the impact of data from radar networks on thunderstorm analysis and forecasting. J. Atmos. Oceanic Technol. 23(1), 46-66.

Xue, M., Hu, M. and Schenkman, A.D., 2014. Numerical prediction of the 8 May 2003 Oklahoma City tornadic supercell and embedded tornado using ARPS with the assimilation of WSR-88D data. Wea. Forecasting 29(1), 39-62.

Yang, J., Zhang, Z., Wei, C., Lu, F. and Guo, Q., 2016. Introducing the new generation of Chinese geostationary weather satellites–FengYun 4 (FY-4). Bull. Amer. Meteor. Soc. (2016).

Zhang, G., 2016. Weather radar polarimetry. CRC Press.

Ziegler, C.L., 2013. A diabatic Lagrangian technique for the analysis of convective storms. Part I: Description and validation via an observing system simulation experiment. J. Atmos. Oceanic Technol. 30(10), 2248-2265.

Zrnić, D.S., Ryzhkov, A., Straka, J., Liu, Y. and Vivekanandan, J., 2001. Testing a procedure for automatic classification of hydrometeor types. J. Atmos. Oceanic Technol. 18(6), 892-913.